Research Article

Nano Research 2019, 12(9): 2218–2223

ISSN 1998-0124 CN 11-5974/O4
https://doi.org/10.1007/s12274-018-2250-2

Co-doped 1T-MoS_2 nanosheets embedded in N, S-doped carbon nanobowls for high-rate and ultra-stable sodium-ion batteries

Peihao Li[1,§], Yong Yang[1,§], Sheng Gong[2], Fan Lv[1], Wei Wang[1], Yiju Li[1], Mingchuan Luo[1], Yi Xing[1], Qian Wang[1,3], and Shaojun Guo[1,4] (✉)

[1] *Department of Materials Science & Engineering, College of Engineering, Peking University, Beijing 100871, China*
[2] *Department of Materials Science and Engineering, Massachusetts Institute of Technology, Cambridge, MA 02139, USA*
[3] *Center for Applied Physics and Technology, College of Engineering, Peking University, Beijing 100871, China*
[4] *BIC-ESAT, College of Engineering, Peking University, Beijing 100871, China*
[§] *Peihao Li and Yong Yang contributed equally to this work.*

Received: 13 September 2018 / **Revised:** 28 October 2018 / **Accepted:** 20 November 2018

ABSTRACT

Despite various 2H-MoS_2/carbon hybrid nanostructures have been constructed and committed to improve the performance for sodium-ion batteries (SIBs), they still show the limited cycle stability due to the relatively large volumetric expansion during the charge–discharge process. Herein, we report the construction of cobalt-doped few-layered 1T-MoS_2 nanosheets embedded in N, S-doped carbon (CMS/NSC) nanobowls derived from metal-organic framework (MOF) precursor via a simple *in situ* sulfurization process. This unique hierarchical structure enables the uniformly dispersed Co-doped 1T-MoS_2 nanosheets intimately couple with the highly conductive carbon nanobowls, thus efficiently preventing the aggregation. In particular, the Co-doping plays a crucial role in maintaining the integrity of structure for MoS_2 during cycling tests, confirmed by first-principles calculations. Compared with pristine MoS_2, the volume deformation of Co-doped MoS_2 can be shrunk by a prominent value of 52% during cycling. Furthermore, the few-layered MoS_2 nanosheets with 1T metallic phase endow higher conductivity, and thus can surpass its counterpart 2H semiconducting phase in battery performance. By virtue of the synergistic effect of stable structure, appropriate doping and high conductivity, the resulting CMS/NSC hybrid shows superior rate capability and cycle stability. The capacity of CMS/NSC can still be 235.9 $mAh \cdot g^{-1}$ even at 25 $A \cdot g^{-1}$, which is 51.3% of the capacity at 0.2 $A \cdot g^{-1}$. Moreover, the capacity can still remain 218.6 $mAh \cdot g^{-1}$ even over 8,240 cycles at 5 $A \cdot g^{-1}$ with a low decay of 0.0044% per cycle, one of the best performances among the reported MoS_2-based anode materials for SIBs.

KEYWORDS

sodium-ion battery, anode, 1T-MoS_2, cobalt-doping, metal-organic framework (MOF)

1 Introduction

Sodium-ion batteries (SIBs) have been deeply investigated as the alternatives to lithium-ion batteries (LIBs) because of the higher abundance and lower cost of sodium [1]. Plenty of work has been committed to achieve a better performance for SIBs [2–4]. Nevertheless, because of the larger radius (2.03 Å compared with 1.34 Å for lithium-ion) and sluggish kinetics of sodium-ion in electrode materials, the performance of SIBs is still unsatisfying and designing applicable electrode materials for SIBs is still an ongoing challenge [5, 6].

With ordered layered structure, graphite has been applied commercially in LIBs. However, sodium can hardly intercalate into pristine graphite due to insufficient interlayered distance and thermodynamic unfavorableness [7]. As an analogue to graphite, MoS_2 is a promising candidate with larger interlayer distance and higher theoretical capacity [8]. The alkali metal ions can be accommodated between the two-dimensional (2D) layers of MoS_2 which are bonded by weak van der Waals force. Specially, the 1T metallic phase of MoS_2 exhibits superior electronic conductivity and more electrochemical reaction sites than its semiconducting counterpart, 2H MoS_2, particularly benefitting the reversible step of conversion reaction below 0.4 V in charge–discharge process [9, 10]. Nonetheless, pure MoS_2 always suffers from poor cycle stability because of the inevitable aggregation and deformation of 2D layers [11]. Thus, proper and rational design of appropriate structure is definitely a significant issue for enhancing electrochemical properties for MoS_2 [12–15]. For example, MoS_2 can be reduced into nanosheets, nanotubes or nanodots due to a better tolerance to volume change during charge–discharge processes and a shortened diffusion distance for ions [16–18]. In addition, combining with carbon base or carbon coating can also be a good way to avoid aggregation and increase conductivity for MoS_2 [19–21]. Recently, metal-organic framework (MOF)-derived material has been drawing increasing attention in energy storage applications in view of its tunable hierarchical structure, diverse heteroatomic doping and high specific area, etc. Multiple structure features, such as nanostructure, carbon coating or heteroatomic doping, can be well maintained and tactically combined from MOF precursor through a simple *in situ* transformation process such as calcination treatment, being capable of reinforcing and stabilizing the metal compound active materials through synergy effect [22]. Thus, suitable and novel structures for MoS_2 can be effectively devised by the force of MOF materials [23, 24]. In particular, notwithstanding the relatively small amount of the introduction of heteroatomic doping into electrode material, it can

---

Address correspondence to guosj@pku.edu.cn

play a decisive role in strengthening the properties of electrode materials by altering and modulating structure [25, 26]. However, such important reinforcement mainly focuses on bringing in heteroatoms into the carbon coating surrounding MoS_2, which typically takes effect by increasing conductivity or providing extra electrochemical active sites for carbon coating [23, 27]. Moreover, despite various carbon-based hybrid architectures with different doping methods have been designed and dedicated to achieve a better cycle stability for MoS_2, the results are still unsatisfactory due to the peripherality of carbon coating that is unable to change the inherent structure feature of MoS_2. On the contrary, the effect of *in situ* metal heteroatomic doping into MoS_2 is seldomly reported and investigated in battery applications, which may be a novel and more valid way to increase the cycling capability for MoS_2 by directly altering the crystallographic structure.

Herein, we synthesized cobalt-doped few-layered MoS_2 nanosheets embedded in N, S-doped carbon (CMS/NSC) nanobowls for boosting SIBs, in which ultra-thin MoS_2 nanosheets are distributed and established uniformly throughout the N, S-doped carbon coating to form a hierarchical and stable structure. In our work, a MOF nanobowl (NB) precursor was selected and converted into CMS/NSC structure through a facile *in situ* sulfurization method. By employing first-principles calculations, Co-doping is found to be the key in enhancing the cycle stability for MoS_2, in which the volume deformation of Co-doped MoS_2 is 52% less than pristine MoS_2 during continuous cycling tests. Moreover, the MoS_2 nanosheets exhibit 1T metallic phase with higher conductivity, rather than traditional 2H-semiconducting phase. Owing to the synergistically cooperative structure and morphology features, the CMS/NSC hybrid was applied as a novel anode material for SIBs, which exhibits excellent rate performance and long-term stability. As a result, the CMS/NSC can yield 459.4 $mAh{\cdot}g^{-1}$ at 0.2 $A{\cdot}g^{-1}$ and can still maintain 235.9 $mAh{\cdot}g^{-1}$ at 25 $A{\cdot}g^{-1}$ (51.3% of the capacity at 0.2 $A{\cdot}g^{-1}$). In addition, the CMS/NSC also demonstrates a superior cycling capability by the capacity retention of 218.6 $mAh{\cdot}g^{-1}$ and 0.0044% capacity loss per cycle over 8,240 cycles at 5 $A{\cdot}g^{-1}$. The present work described can facilitate the development of hybrid materials for boosting the performance of SIBs by rational structure architecture and proper ionic doping.

2 Experimental

2.1 Synthesis of NB precursor

Typically, 0.25 mL H_3BTC (60 mg/mL, DMF), 0.25 mL thioacetamide (20 mg/mL, DMF), 0.5 mL PVP (40 mg/mL, DMF), 1 mL hexamethylenetetramine (20 mg/mL, EtOH), 1 mL $Co(acac)_3$ (9 mg/mL, DMF) and 0.06 mL $(NH_4)_6Mo_7O_{24}{\cdot}4H_2O$ (150 mg/mL, H_2O) were mixed with 5 mL DMF to form a homogeneous solution. In a 25 mL Teflon-lined stainless-steel autoclave, the temperature was raised to 180 °C rapidly from room temperature and then kept for 12 h in an oven. After the solution was cooled down naturally to room temperature, the precipitate product was washed by EtOH for several times.

2.2 Synthesis of CMS/NSC

CMS/NSC was synthesized by the *in situ* sulfurization treatment of NB precursor. Typically, NB precursor and sulfur powder were both placed in a tube-type Muffle furnace with the mass ratio of 1:8. Under the nitrogen atmosphere, the furnace was heated from ambient temperature to 600 °C at a ramp rate of 4.75 $°C{\cdot}min^{-1}$, then held at 600 °C for 3 h before cooling down to room temperature naturally.

2.3 Structural and physical characterizations

Field emission scanning electron microscopy (FESEM, JEOL, JSM-6701F) and transmission electron microscope (TEM, JEOL, JEM-2010) were both employed to observe the morphology of active materials. The elemental information of active materials was characterized by an energy-dispersive X-ray (EDX) spectrometer (Bruker Quantax), inductively coupled plasma atomic emission spectroscopy (ICP-AES, Agilent 8800) and Elementar Vario EL CUBE. The crystallographic structure was measured by X-ray diffraction measurements (XRD, Rigaku, D/max-RB). X-ray photoelectron spectroscopy (XPS) measurements were conducted using an AXIS-Ultra instrument from Kratos Analytical using monochromatic Al Kα radiation (225 W, 15 mA, 15 kV) and low-energy electron flooding for charge compensation. The Raman spectra were measured by an iHR550 Raman microscope using a laser with excitation wavelength of 532 nm at room temperature. The N_2 adsorption–desorption isotherms were performed using an automated gas sorption analyzer (Autosorb-iQ-2MP, Quantachrome, USA).

2.4 Electrochemical measurements

The CMS/NSC was mixed with acetylene black as conductive additive and polyvinylidene fluoride (PVDF) as binder in N-methylpyrrolidone (NMP) with the weight ratio of 7:2:1. After stirring 12 h, the obtained slurry was applied onto a copper foil as current collector and dried at 80 °C for 12 h under vacuum. The copper foil covered with active materials was cut into electrode slices using a tablet machine, which were then assembled into CR2032 coin-type half-cells in an argon-filled glove box under a strict condition where the concentration of O_2 and H_2O are both below 0.1 ppm. Sodium metal foil was applied as both counter and reference electrodes. The electrolyte solution used was 1.0 M sodium hexafluorophosphate ($NaPF_6$) in 1:1 (volume ratio) ethylene carbonate (EC) and diethyl carbonate (DEC). The glass fibber (GF/D) from Whatman was employed as the separator for SIBs. Galvanostatic charge–discharge processes were performed using the LAND-CT2011A battery-testing instrument at room temperature at various current densities from 0.01 to 2.5 V. Cyclic voltammetry (CV, CHI 660e) was conducted at different scan rates between 0.01 and 2.5 V.

2.5 Computational methods

All the first-principles calculations were conducted by density functional theory (DFT) implemented in the Vienna *ab initio* simulation package (VASP) [28]. The projector augmented wave (PAW) scheme [29] is used with a kinetic energy cutoff of 600 eV. The first Brillouin zone is sampled by a $5 \times 5 \times 2$ k-point grid within the Monkhorst–Pack scheme [30]. The exchange-correlation interaction is treated by Perdew–Burke–Ernzerh functional (PBE) within global gradient approximation (GGA) [31–34]. All the calculations are spin polarized. The convergence criteria of 10^{-4} eV and 10^{-2} eV/Å are used for the total energy and atomic forces, respectively.

3 Results and discussion

In a typical synthesis procedure, the NB precursor was synthesized through a hydrothermal method [35]. Then the dried NB precursor was calcinated together with sulfur powder under the atmosphere of nitrogen at 600 °C for 3 h to obtain CMS/NSC. SEM and TEM were employed to investigate the morphology of NB precursor and CMS/NSC. Figures S1 and S2 in the Electronic Supplementary Material (ESM) show the SEM and TEM images of NB precursor. The magnified SEM and TEM images in Figs. 1(a)–(c) reveal that the NB precursor with a bowl-like shape has the diameter of 200–300 nm. The corresponding three-dimensional (3D) structure scheme for NB precursor is shown in the inset of Fig. 1(a). Furthermore, Fig. S3 in the ESM displays the XRD pattern of obtained NB precursor. The $(2, \bar{1}, 0)$ peak is accordant with the reported

Co-BTC MOFs [35, 36]. The bowl-like morphology of CMS/NSC can be maintained well after sulfurization process, verified by the SEM images (Figs. 1(d), 1(e), and Fig. S4 in the ESM) and TEM image (Fig. 1(f)), nonetheless, the surface texture of CMS/NSC has been changed. As shown in Fig. S5 in the ESM, uniformly dispersed little fringes are observed in CMS/NSC in white circles, attributed to the generation of MoS_2 nanosheets after sulfurization. Likewise, the inset of Fig. 1(d) and Fig. S5 in the ESM illustrate a 3D model of MoS_2 sheets embedded in carbon nanobowl.

To further probe the morphology of MoS_2 nanosheets in CMS/NSC, the high-resolution transmission electron microscopy (HRTEM) was conducted. Figures 1(g), 1(h), and Fig. S6 in the ESM clearly mark the (002) and (100) planes of MoS_2, and confirm the few-layered ultrathin nanosheet nature of MoS_2 in CMS/NSC. Figure S7 in the ESM presents the corresponding XRD pattern of CMS/NSC. The obscurity of (002) peak is in conformity with the few-layered ultrathin morphology [37]. The scanning transmission electron microscopy (STEM) image and corresponding energy dispersive X-ray spectrometry (EDX) are shown in Figs. 1(i) and 1(j), confirming the element distribution in CMS/NSC, which is also in agreement with the EDX spectrum (Fig. S8 in the ESM) and the line scanning analysis (Fig. S9 in the ESM). The Co, Mo, S, N and C distribute uniformly throughout the CMS/NSC. In addition, the weight ratio of Co:Mo is 0.27:1, measured by inductively coupled plasma atomic emission spectroscopy (ICP-AES). The N, S-doped carbon coating around MoS_2 nanosheets can avoid the aggregation and increase the conductivity for MoS_2 nanosheets [38]. The N and S heteroatoms can also create extra sites for facilitating capacitive process during electrochemical tests. The organic elemental analysis indicates that the weight ratio of H, C, and N is 3.40%, 17.01%, and 3.95%, respectively. Besides, the D:G ratio of 0.84 in the Raman spectrum (Fig. S10 in the ESM) indicates a high graphitization degree for carbon coating [39].

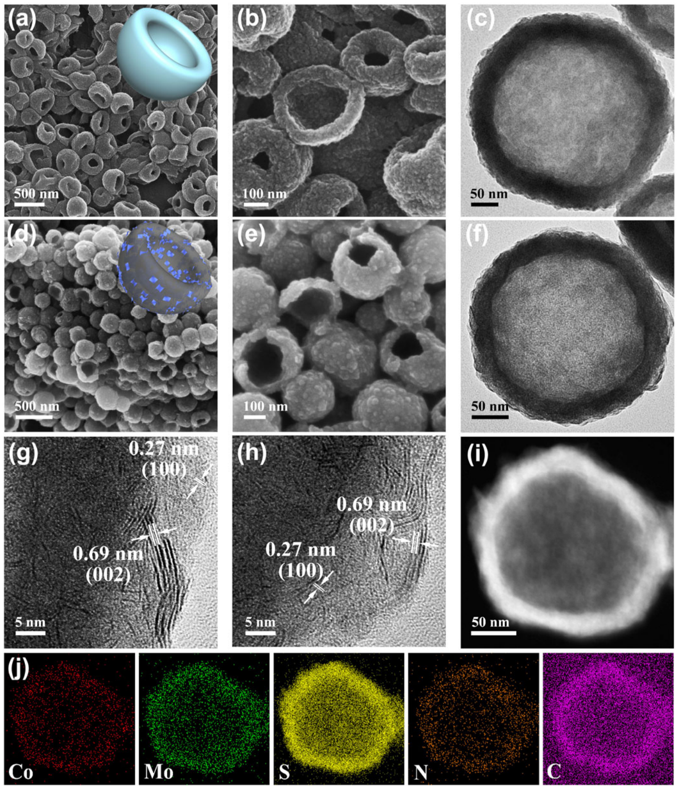

Figure 1 (a) and (b) SEM images and (c) TEM image of NB precursor. Inset of (a) is the 3D scheme for NB precursor. (d) and (e) SEM images and (f) TEM image of CMS/NSC. Inset of (d) is the 3D model for CMS/NSC. (g) and (h) HRTEM images of CMS/NSC. (i) STEM image of CMS/NSC and the corresponding (j) EDX mapping of CMS/NSC.

XPS was carried out to determine the chemical state of Co-doped MoS_2 nanosheets (Fig. S11 in the ESM). Figure 2(a) shows the high-resolution XPS for Mo 3d doublets (Mo $3d_{3/2}$ and $3d_{5/2}$) with the binding energy of 232.7 and 229.3 eV, ascribed to Mo^{4+}. However, the peak located at 236.2 eV is due to the presence of Mo^{6+} $3d_{5/2}$ of MoO_3, indicating the ineluctable surface oxidation of MoS_2. Another peak centered at 226.6 eV is assigned to S 2s, and the peaks at 163.5 and 162.1 eV in Fig. 2(b) are attributed to the S $2p_{1/2}$ and S $2p_{3/2}$ of S^{2-}. In addition, Fig. 2(c) presents the XPS spectrum of Co 2p. The blue peak doublets located at 794.3 and 779.4 eV are due to the $2p_{1/2}$ and $2p_{3/2}$ of CoMoS, while the doublets at 798.3 and 782.1 eV belong to Co^{II} $2p_{1/2}$ and Co^{II} $2p_{3/2}$. The remaining peaks come from peak satellite signals [40, 41]. Moreover, Raman spectrum of MoS_2 in CMS/NSC in Fig. 2(d) further confirms the 1T metallic phase by showing two Raman shift peaks at 186 and 339 cm^{-1} [42]. The 1T metallic phase of MoS_2 plays an important role in boosting battery performance such as rate capability because of its higher electronic conductivity and more reaction sites than its counterpart 2H semiconducting phase, especially promoting the kinetics of reversible conversion reaction below 0.4 V during successive sodiation–desodiation process [9, 10, 43]. Nitrogen adsorption–desorption was employed to study the surface area and porous texture of CMS/NCS, as displayed in Fig. S12 in the ESM. Type IV isotherms (IUPAC definition) with type H3 hysteresis loops are recognized (Fig. S12(a) in the ESM), indicating the presence of mesopores. The Brunauer–Emmett–Teller (BET) surface area is calculated to be 134 $m^2 \cdot g^{-1}$. The corresponding pore size distribution (Fig. S12(b) in the ESM) demonstrates that the mesopores are mainly centered at 2.8 and 4 nm. High specific area and mesoporous structure can reduce the travel distance for ions as well as benefit the penetration of electrolyte.

The electrochemical performance of CMS/NSC was investigated by CV and galvanostatic tests. Figure 3(a) presents the CV curves for CMS/NSC in the first 5 cycles over a potential window of 0.01–2.5 V (vs. Na^+/Na) at a scan rate of 0.1 $mV \cdot s^{-1}$. In the 1st cycle, the irreversible cathodic peaks located at 0.98, 0.75 and 0.17 V are due to the intercalation of sodium, the formation of solid-electrolyte interface (SEI) film, and the final conversion to Mo and Na_2S, respectively [44]. From the second cycle, these three peaks disappear, indicating a new electrochemical mechanism in the following cycles. As reported in the previous work, the redox peaks above 0.4 V are attributed to the intercalation-deintercalation of sodium, while the ones below 0.4 V correspond to the reversible conversion reaction [10, 45]. The CV curves in the subsequent cycles

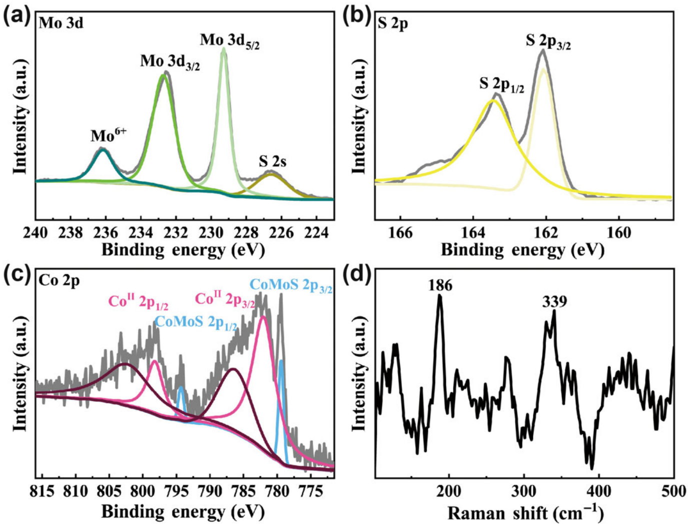

Figure 2 High-resolution XPS spectra of (a) Mo 3d peaks, (b) S 2p peaks and (c) Co 2p peaks. (d) Raman spectrum of 1T-MoS_2 in CMS/NSC.

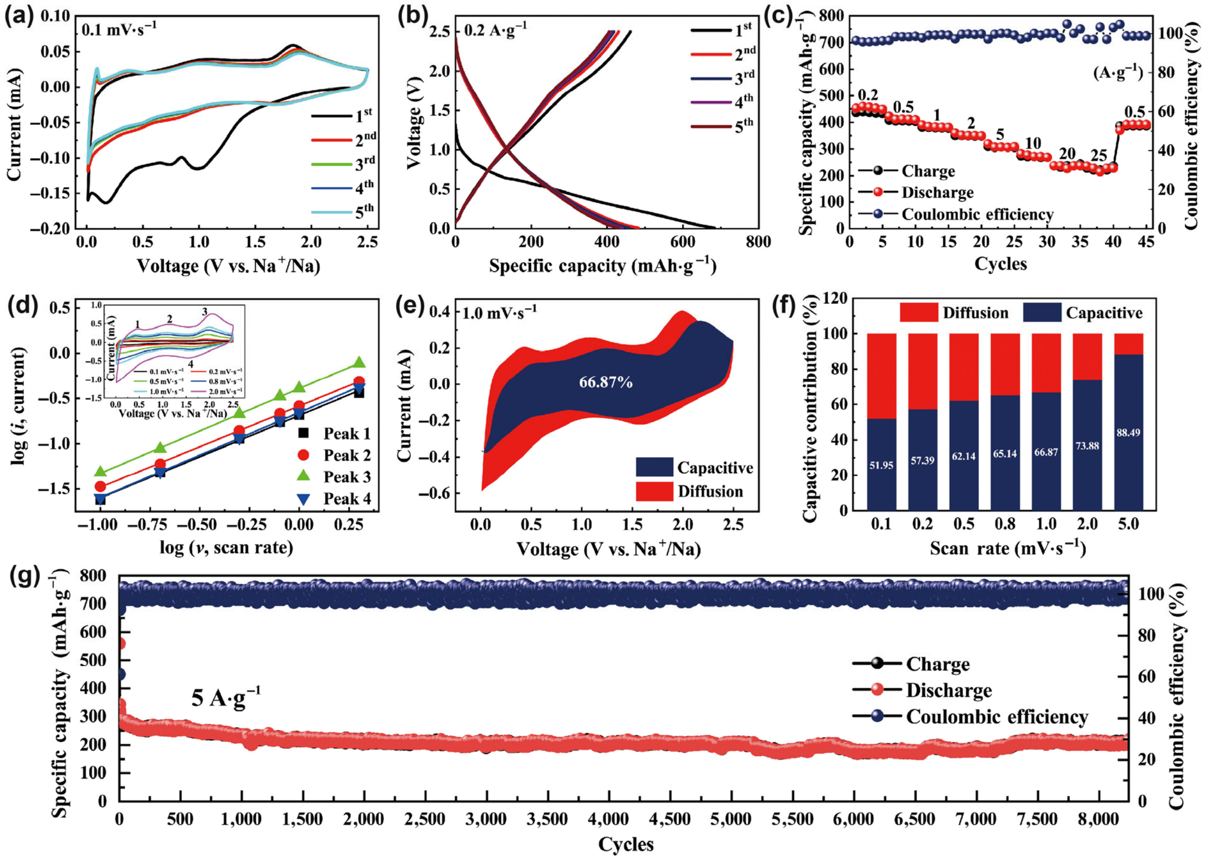

Figure 3 (a) CV curves for CMS/NSC in the first five cycles at a scan rate of 0.1 mV·s⁻¹. (b) Charge–discharge profiles for CMS/NSC at 0.2 A· g⁻¹ in the first five cycles. (c) Rate capability of CMS/NSC at various current densities from 0.2 to 25 A·g⁻¹. (d) log(i) versus log(v) based on specific peak currents from the CV curves at different scan rates from 0.1 to 2.0 mV·s⁻¹ (inset). (e) CV curve with the pseudocapacitive contribution shown in the blue region at a scan rate of 1.0 mV·s⁻¹. (f) The bar chart shows the contribution ratios of capacitive capacity and diffusion-limited capacity at various scan rates. (g) Long-term cycle performance of CMS/NSC at 5 A·g⁻¹ over 8,240 cycles.

nearly override, indicating good reversibility. Figure 3(b) shows the charge–discharge profiles for CMS/NSC in the first five cycles at 0.2 A·g⁻¹. In the 1st cycle, the CMS/NSC yields an irreversible discharge capacity of 683.4 mAh·g⁻¹ and low Coulombic efficiency (CE) of 67.5%, attributed to the formation of SEI film and the decomposition of electrolyte [3]. The discharge voltage plateau located at 0.75 V in the 1st cycle, which disappears in the following cycles, is in accordance with the cathodic peak at 0.75 V in the 1st CV curve in Fig. 3(a). In the following cycles, the charge–discharge profiles overlap well and no obvious fading is observed.

The excellent rate capability of CMS/NSC is displayed in Fig. 3(c). The CMS/NSC can deliver a discharge capacity of 459.4, 422.8, 390.4, 360.1, 319.1, 282.2, 238.2, 235.9 mAh·g⁻¹ at 0.2, 0.5, 1, 2, 5, 10, 20 and 25 A·g⁻¹, respectively. After the current density returns to 0.5 A·g⁻¹, a capacity of 391.9 mAh·g⁻¹ can still be maintained. In order to account for the outstanding rate capability, pseudocapacitive behavior of CMS/NSC was investigated by CV at different scan rates. As presented in the inset of Fig. 3(d), 4 peak currents (i) and 5 scan rates (v) are selected to evaluate the electrochemical kinetics process using the following equation [46]

$$i = av^b \tag{1}$$

where a and b represent the empirical parameters. The b value of 0.5 indicates an ideal diffusion-controlled behavior, while 1.0 stands for a capacitive one. The linear relationships between log(i) and log(v) are demonstrated in Fig. 4(d). The slopes, that is, the b values for four peaks were calculated to be 0.91, 0.90, 0.94 and 0.94, indicating a capacitive process. To further quantify the capacitive contribution for CMS/NSC, the current was divided at a fixed voltage (V) based on the following equation [47, 48]

$$i(V) = k_1v + k_2v^{1/2} \tag{2}$$

where k_1v stands for capacitive contribution, whereas $k_2v^{1/2}$ represents diffusion-controlled contribution. Then Eq. (2) can be converted to

$$i(V)/v^{1/2} = k_1v^{1/2} + k_2 \tag{3}$$

The parameter k_1 can be calculated from the linear relationship between $i(V)/v^{1/2}$ and $v^{1/2}$. Therefore, the capacitive current k_1v can be obtained facilely at each fixed voltage (V). Finally, the ratio of the area inside the capacitive CV curve and that of the original CV curve is the capacitive contribution. Figure 3(e) shows the CVs with the capacitive contribution of 66.87% (the blue region) at a scan rate of 1 mV·s⁻¹. In addition, Fig. S13 in the ESM also displays the capacitive contribution in CV curve at other scan rates. The corresponding bar chart of the contribution ratios of capacitive behavior at various scan rates is presented in Fig. 3(f), where capacitive contribution shows positive correlation with scan rate. The result indicates that capacitive behavior plays an important role in boosting the rate performance of CMS/NSC. Figure 3(g) displays the long-term cycling performance for CMS/NSC. At a high current density of 5 A·g⁻¹, a capacity of 218.6 mAh·g⁻¹ can still be maintained over 8,240 cycles with a very low decay of 0.0044% per cycle and CE of 100%, which demonstrates a superior cycle stability than other reported MoS_2-based SIB anode materials (Table S1 in the ESM).

To get insight into the high cycle stability of the CMS/NSC, first-principles calculations are performed to measure the degree of structural deformation, which is demonstrated to be crucial for the stability of electrodes [49–51]. We build the Co-doped MoS_2 model

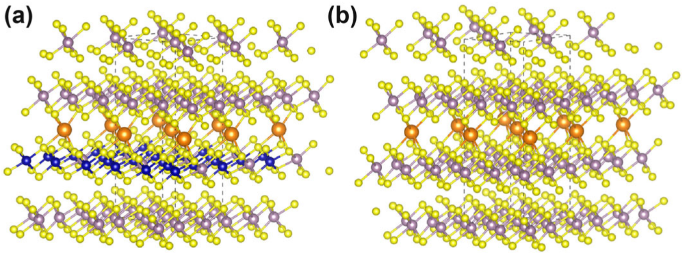

Figure 4 Configurations of Na inserted in (a) Co-doped MoS_2 and (b) pristine MoS_2, respectively. Color coding: yellow: S; pink: Mo; blue: Co; orange: Na.

and several trial doping structures then select the one with the lowest energy for further calculation. For both Co-doped and pristine MoS_2 structures, as shown in Fig. 4, we introduce one Na atom into the two systems, and we find that the volume only expands 4.88% for the Co-doped MoS_2, much lower than that of the commercial graphite anode for LIBs (around 10%), while that of the pristine MoS_2 is 10.1%. Thus, the volume deformation of Co-doped MoS_2 is calculated to be 52% lower than the one of pristine MoS_2. To best of our knowledge, it is the first time that the effect of Co-doping in MoS_2 has been studied in batteries. This significant decrease of volume expansion can well explain the improvement of cycling capability of MoS_2 after Co-doping [52].

4 Conclusions

In summary, we demonstrate a facile *in situ* sulfurization method for making hierarchical CMS/NSC hybrid composed of few-layered Co-doped 1T-MoS_2 nanosheets as an outstanding anode material for SIBs. First-principles calculations reveal that Co-doping can reduce the volume deformation by a high value of 52% for MoS_2 during successive sodium-ion intercalation-extraction processes, thus bringing about an extraordinary cycle stability. Moreover, the 1T metallic phase of MoS_2 confirmed in CMS/NSC contributes a higher conductivity, leading to a better electrochemical property than rival 2H semiconducting phase. Additionally, the morphology of ultrathin nanosheets with just a few layers can provide remarkably shortened diffusion distance for ions, and the nature of aggregation of nanomaterials can be well avoided by N, S-doped carbon coating, which can also further increase the conductivity for MoS_2 nanosheets. As a result of synergy effect of Co-doping, high conductivity and stable architecture, the CMS/NSC can achieve 459.4 $mAh\cdot g^{-1}$ at 0.2 $A\cdot g^{-1}$ and still keep 235.9 $mAh\cdot g^{-1}$ at a high current density of 25 $A\cdot g^{-1}$, corroborated by the high pseudocapacitive contribution (88.49% at 5 $mV\cdot s^{-1}$) derived from CV study. In addition, at 5 $A\cdot g^{-1}$, a reversible capacity of 218.6 $mAh\cdot g^{-1}$ can still be obtained even after 8,240 cycles, corresponding to 0.0044% decay per cycle during continuous cycling processes. The present work paves ways for the reasonable design of electrode materials with integrated high performance.

Acknowledgements

This work was financially supported by the National Key R&D Program of China (No. 2016YFB0100200), Young Thousand Talents Program, the Open Project Foundation of State Key Laboratory of Chemical Resource Engineering, the China Postdoctoral Science Foundation (No. 2017M610018), the National Natural Science Foundation of China (No. 51671003), Start-up Funding from Peking University.

Electronic Supplementary Material: Supplementary material (SEM images, TEM images, XRD patterns, EDX spectrum, Raman spectrum, XPS spectrum, BET analysis, CV curves, and table for comparison) is available in the online version of this article at https://doi.org/10.1007/s12274-018-2250-2.

References

[1] Delmas, C. Sodium and sodium-ion batteries: 50 years of research. *Adv. Energy Mater*. **2018**, *8*, 1703137.

[2] Wang, W.; Li, P. H.; Zheng, H.; Liu, Q.; Lv, F.; Wu, J. D.; Wang, H.; Guo, S. J. Ultrathin layered SnSe nanoplates for low voltage, high-rate, and long-life alkali-ion batteries. *Small* **2017**, *13*, 1702228.

[3] Yang, Y.; Luo, M. C.; Xing, Y.; Wang, S. T.; Zhang, W. Y.; Lv, F.; Li, Y. J.; Zhang, Y. L.; Wang, W.; Guo, S. J. A universal strategy for intimately coupled carbon nanosheets/MoM nanocrystals (M = P, S, C, and O) hierarchical hollow nanospheres for hydrogen evolution catalysis and sodium-ion storage. *Adv. Mater*. **2018**, *30*, 1706085.

[4] Chayambuka, K.; Mulder, G.; Danilov, D. L.; Notten, P. H. L. Sodium-ion battery materials and electrochemical properties reviewed. *Adv. Energy Mater*. **2018**, *8*, 1800079.

[5] Hwang, J. Y.; Myung, S. T.; Sun, Y. K. Sodium-ion batteries: Present and future. *Chem. Soc. Rev*. **2017**, *46*, 3529–3614.

[6] Li, P. H.; Wang, W.; Gong, S.; Lv, F.; Huang, H. X.; Luo, M. C.; Yang, Y.; Yang, C.; Zhou, J. H.; Qian, C. et al. Hydrogenated $Na_2Ti_3O_7$ epitaxially grown on flexible N-doped carbon sponge for potassium-ion batteries. *ACS Appl. Mater. Interfaces* **2018**, *10*, 37974–37980.

[7] Wen, Y.; He, K.; Zhu, Y. J.; Han, F. D.; Xu, Y. H.; Matsuda, I.; Ishii, Y.; Cumings, J.; Wang, C. S. Expanded graphite as superior anode for sodium-ion batteries. *Nat. Commun*. **2014**, *5*, 4033.

[8] Yang, Y.; Wang, S. T.; Lin, S.; Li, Y. T.; Zhang, W. Y.; Chao, Y. G.; Luo, M. C.; Xing, Y.; Wang, K.; Yang, C. et al. Rational design of hierarchical TiO_2/epitaxially aligned MoS_2–carbon coupled interface nanosheets core/shell architecture for ultrastable sodium-ion and lithium-sulfur batteries. *Small Methods* **2018**, *16*, 1800119.

[9] Lei, Z. D.; Zhan, J.; Tang, L.; Zhang, Y.; Wang, Y. Recent development of metallic (1T) phase of molybdenum disulfide for energy conversion and storage. *Adv. Energy Mater*. **2018**, *8*, 1703482.

[10] Sun, D.; Ye, D. L.; Liu, P.; Tang, Y. G.; Guo, J.; Wang, L. Z.; Wang, H. Y. MoS_2/graphene nanosheets from commercial bulky MoS_2 and graphite as anode materials for high rate sodium-ion batteries. *Adv. Energy Mater*. **2018**, *8*, 1702383.

[11] Park, J.; Kim, J. S.; Park, J. W.; Nam, T. H.; Kim, K. W.; Ahn, J. H.; Wang, G. X.; Ahn, H. J. Discharge mechanism of MoS_2 for sodium ion battery: Electrochemical measurements and characterization. *Electrochim. Acta* **2013**, *92*, 427–432.

[12] Xing, Y.; Yang, Y.; Chen, R. J.; Luo, M. C.; Chen, N.; Ye, Y. S.; Qian, J.; Li, L.; Wu, F.; Guo, S. J. Strongly coupled carbon nanosheets/molybdenum carbide nanocluster hollow nanospheres for high-performance aprotic Li-O_2 battery. *Small* **2018**, *14*, 1704366.

[13] Yang, Y.; Wang, S. T.; Jiang, C. H.; Lu, Q. C.; Tang, Z. L.; Wang, X. Controlled synthesis of hollow Co–Mo mixed oxide nanostructures and their electrocatalytic and lithium storage properties. *Chem. Mater*. **2016**, *28*, 2417–2423.

[14] Yang, Y.; Wang, S. T.; Luo, M. C.; Wang, W.; Lv, F.; Tang, Z. L.; Guo, S. J. $Li_4Ti_5O_{12}$–TiO_2/MoO_2 nanoclusters-embedded into carbon nanosheets core/shell porous superstructures boost lithium ion storage. *J. Mater. Chem. A* **2017**, *5*, 12096–12102.

[15] Yang, Y.; Wang, S. T.; Zhang, J. C.; Li, H. Y.; Tang, Z. L.; Wang, X. Nanosheet-assembled $MoSe_2$ and S-doped $MoSe_{2-x}$ nanostructures for superior lithium storage properties and hydrogen evolution reactions. *Inorg. Chem. Front*. **2015**, *2*, 931–937.

[16] Jiao, Y. C.; Mukhopadhyay, A.; Ma, Y.; Yang, L.; Hafez, A. M.; Zhu, H. L. Ion transport nanotube assembled with vertically aligned metallic MoS_2 for high rate lithium-ion batteries. *Adv. Energy Mater*. **2018**, *8*, 1702779.

[17] Xie, X. Q.; Makaryan, T.; Zhao, M. Q.; Van Aken, K. L.; Gogotsi, Y.; Wang, G. X. MoS_2 nanosheets vertically aligned on carbon paper: A freestanding electrode for highly reversible sodium-ion batteries. *Adv. Energy Mater*. **2016**, *6*, 1502161.

[18] Sun, W. Y.; Li, P.; Liu, X.; Shi, J. J.; Sun, H. M.; Tao, Z. L.; Li, F. J.; Chen, J. Size-controlled MoS_2 nanodots supported on reduced graphene oxide for hydrogen evolution reaction and sodium-ion batteries. *Nano Res*. **2017**, *10*, 2210–2222.

[19] Yang, H.; Wang, M.; Liu, X. W.; Jiang, Y.; Yu, Y. MoS_2 embedded in 3D interconnected carbon nanofiber film as a free-standing anode for sodium-ion batteries. *Nano Res*. **2018**, *11*, 3844–3853.

[20] Yang, Q. Q.; Liu, M. C.; Hu, Y. M.; Xu, Y.; Kong, L. B.; Kang, L. Facile synthesis of MoS_2/graphite intercalated composite with enhanced electrochemical performance for sodium ion battery. *J. Energy Chem*. **2018**, *27*, 1208–1213.

[21] Lu, B.; Liu, J.; Hu, R. Z.; Wang, H.; Li, J. W.; Zhu, M. C@MoS_2@PPy sandwich-like nanotube arrays as an ultrastable and high-rate flexible anode for Li/Na-ion batteries. *Energy Storage Mater*. **2018**, *14*, 118–128.

[22] Xia, W.; Mahmood, A.; Zou, R. Q.; Xu, Q. Metal-organic frameworks and their derived nanostructures for electrochemical energy storage and conversion. *Energy Environ. Sci*. **2015**, *8*, 1837–1866.

[23] Ren, W. N.; Zhang, H. F.; Guan, C.; Cheng, C. W. Ultrathin MoS_2 nanosheets@metal organic framework-derived N-doped carbon nanowall arrays as sodium ion battery anode with superior cycling life and rate capability. *Adv. Funct. Mater*. **2017**, *27*, 1702116.

[24] Wang, Y. Y.; Kang, W. P.; Cao, D. W.; Zhang, M. H.; Kang, Z. X.; Xiao, Z. Y.; Wang, R. M.; Sun, D. F. A yolk-shelled Co_9S_8/MoS_2-CN nanocomposite derived from a metal-organic framework as a high performance anode for sodium ion batteries. *J. Mater. Chem. A* **2018**, *6*, 4776–4782.

[25] Wang, X. L.; Li, G.; Seo, M. H.; Hassan, F. M.; Hoque, M. A.; Chen, Z. W. Sulfur atoms bridging few-layered MoS_2 with S-doped graphene enable highly robust anode for lithium-ion batteries. *Adv. Energy Mater*. **2015**, *5*, 1501106.

[26] Chen, B.; Meng, Y. H.; He, F.; Liu, E. Z.; Shi, C. S.; He, C. N.; Ma, L. Y.; Li, Q. Y.; Li, J. J.; Zhao, N. Q. Thermal decomposition-reduced layer-by-layer nitrogen-doped graphene/MoS_2/nitrogen-doped graphene heterostructure for promising lithium-ion batteries. *Nano Energy* **2017**, *41*, 154–163.

[27] Li, P.; Jeong, J. Y.; Jin, B. J.; Zhang, K.; Park, J. H. Vertically oriented MoS_2 with spatially controlled geometry on nitrogenous graphene sheets for high-performance sodium-ion batteries. *Adv. Energy Mater*. **2018**, *8*, 1703300.

[28] Kresse, G.; Furthmuller, J. Efficient iterative schemes for *ab initio* total-energy calculations using a plane-wave basis set. *Phys. Rev. B* **1996**, *54*, 11169–11186.

[29] Blöchl, P. E. Projector augmented-wave method. *Phys. Rev. B* **1994**, *50*, 17953–17979.

[30] Monkhorst, H. J.; Pack, J. D. Special points for brillouin-zone integrations. *Phys. Rev. B* **1976**, *13*, 5188–5192.

[31] Perdew, J. P.; Burke, K.; Ernzerhof, M. Generalized gradient approximation made simple. *Phys. Rev. Lett*. **1996**, *77*, 3865–3868.

[32] Mortazavi, M.; Wang, C.; Deng, J. K.; Shenoy, V. B.; Medhekar, N. V. *Ab initio* characterization of layered MoS_2 as anode for sodium-ion batteries. *J. Power Sources* **2014**, *268*, 279–286.

[33] Deng, J.; Li, H. B.; Wang, S. H.; Ding, D.; Chen, M. S.; Liu, C.; Tian, Z. Q.; Novoselov, K. S.; Ma, C.; Deng, D. H. et al. Multiscale structural and electronic control of molybdenum disulfide foam for highly efficient hydrogen production. *Nat. Commun*. **2017**, *8*, 14430.

[34] Duerloo, K. A. N.; Li, Y.; Reed, E. J. Structural phase transitions in two-dimensional Mo- and W-dichalcogenide monolayers. *Nat. Commun*. **2014**, *5*, 4214.

[35] He, T.; Xu, X. B.; Ni, B.; Lin, H. F.; Li, C. Z.; Hu, W. P.; Wang, X. Metal-organic framework based microcapsules. *Angew. Chem*. **2018**, *130*, 10305–10309.

[36] Gao, C. Y.; Liu, S. X.; Xie, L. H.; Ren, Y. H.; Cao, J. F.; Sun, C. Y. Design and construction of a microporous metal-organic framework based on the pillared-layer motif. *Crystengcomm* **2007**, *9*, 545–547.

[37] Zhang, P.; Qin, F. R.; Zou, L.; Wang, M. R.; Zhang, K.; Lai, Y. Q.; Li, J. Few-layered MoS_2/C with expanding *d*-spacing as a high-performance anode for sodium-ion batteries. *Nanoscale* **2017**, *9*, 12189–12195.

[38] Wang, F.; Zhuo, H. Y.; Han, X. G.; Chen, W. M.; Sun, D. Foam-like CoO@N,S-codoped carbon composites derived from a well-designed N,S-rich Co-MOF for lithium-ion batteries. *J. Mater. Chem. A* **2017**, *5*, 22964–22969.

[39] Yue, H. Y.; Shi, Z. P.; Wang, Q. X.; Cao, Z. X.; Dong, H. Y.; Qiao, Y.; Yin, Y. H.; Yang, S. T. MOF-derived cobalt-doped ZnO@C composites as a high-performance anode material for lithium-ion batteries. *ACS Appl. Mater. Interfaces* **2014**, *6*, 17067–17074.

[40] Zheng, F.; Huang, N.; Peng, R. C.; Ding, Y. Y.; Li, G. W.; Xia, Z. F.; Sun, P. P.; Sun, X. H.; Geng, J. G. Cobalt-doped molybdenum disulfide *in-situ* grown on graphite paper with excellent electrocatalytic activity for triiodide evolution. *Electrochim. Acta* **2018**, *263*, 328–337.

[41] Liu, G. L.; Robertson, A. W.; Li, M. M. J.; Kuo, W. C. H.; Darby, M. T.; Muhieddine, M. H.; Lin, Y. C.; Suenaga, K.; Stamatakis, M.; Warner, J. H. et al. MoS_2 monolayer catalyst doped with isolated Co atoms for the hydrodeoxygenation reaction. *Nat. Chem*. **2017**, *9*, 810–816.

[42] Geng, X. M.; Jiao, Y. C.; Han, Y.; Mukhopadhyay, A.; Yang, L.; Zhu, H. L. Freestanding metallic 1T MoS_2 with dual ion diffusion paths as high rate anode for sodium-ion batteries. *Adv. Funct. Mater*. **2017**, *27*, 1702998.

[43] Acerce, M.; Voiry, D.; Chhowalla, M. Metallic 1T phase MoS_2 nanosheets as supercapacitor electrode materials. *Nat. Nanotechnol*. **2015**, *10*, 313–318.

[44] Wu, J. X.; Lu, Z. H.; Li, K. K.; Cui, J.; Yao, S. S.; Haq, M. I. U.; Li, B. H.; Yang, Q. H.; Kang, F. Y.; Ciucci, F. et al. Hierarchical MoS_2/carbon microspheres as long-life and high-rate anodes for sodium-ion batteries. *J. Mater. Chem. A* **2018**, *6*, 5668–5677.

[45] Hu, Z.; Wang, L. X.; Zhang, K.; Wang, J. B.; Cheng, F. Y.; Tao, Z. L.; Chen, J. MoS_2 nanoflowers with expanded interlayers as high-performance anodes for sodium-ion batteries. *Angew. Chem., Int. Ed*. **2014**, *53*, 12794–12798.

[46] Yang, C.; Feng, J. R.; Lv, F.; Zhou, J. H.; Lin, C. F.; Wang, K.; Zhang, Y. L.; Yang, Y.; Wang, W.; Li, J. B. et al. Metallic graphene-like VSe_2 ultrathin nanosheets: Superior potassium-ion storage and their working mechanism. *Adv. Mater*. **2018**, *30*, 1800036.

[47] Wang, W.; Jiang, B.; Qian, C.; Lv, F.; Feng, J. R.; Zhou, J. H.; Wang, K.; Yang, C.; Yang, Y.; Guo, S. J. Pistachio-shuck-like $MoSe_2$/C core/shell nanostructures for high-performance potassium-ion storage. *Adv. Mater*. **2018**, *30*, 1801812.

[48] Xiao, Y. H.; Su, D. C.; Wang, X. Z.; Wu, S. D.; Zhou, L. M.; Shi, Y.; Fang, S. M.; Cheng, H. M.; Li, F. CuS microspheres with tunable interlayer space and micropore as a high-rate and long-life anode for sodium-ion batteries. *Adv. Energy Mater*. **2018**, *8*, 1800930.

[49] Gong, S.; Wang, Q. Boron-doped graphene as a promising anode material for potassium-ion batteries with a large capacity, high rate performance, and good cycling stability. *J. Phys. Chem. C* **2017**, *121*, 24418–24424.

[50] Aricò, A. S.; Bruce, P.; Scrosati, B.; Tarascon, J. M.; Van Schalkwijk, W. Nanostructured materials for advanced energy conversion and storage devices. *Nat. Mater*. **2005**, *4*, 366–377.

[51] Winter, M.; Besenhard, J. O. Electrochemical lithiation of tin and tin-based intermetallics and composites. *Electrochim. Acta* **1999**, *45*, 31–50.

[52] Kim, H.; Park, I.; Lee, S.; Kim, H.; Park, K. Y.; Park, Y. U.; Kim, H.; Kim, J.; Lim, H. D.; Yoon, W. S. et al. Understanding the electrochemical mechanism of the new iron-based mixed-phosphate $Na_4Fe_3(PO_4)_2(P_2O_7)$ in a Na rechargeable battery. *Chem. Mater*. **2013**, *25*, 3614–3622.